

NANO EXPRESS

Open Access



Preparation of $\text{SnIn}_4\text{S}_8/\text{TiO}_2$ Nanotube Photoanode and Its Photocathodic Protection for Q235 Carbon Steel Under Visible Light

Hong Li^{1*}, Weizhe Song¹, Xingqiang Cui¹, Yanhui Li¹, Baorong Hou^{2,3}, Lianjun Cheng¹ and Pengfei Zhang¹

Abstract

TiO_2 is an attractive semiconductor suitable for photocathodic protection, but its weak absorption of visible light and low quantum yield limit its usage. Here, a new heterostructured SnIn_4S_8 nanosheet/ TiO_2 nanotube photoanode was prepared and its photocathodic protection performance was analyzed. SnIn_4S_8 nanosheets were uniformly deposited on the surface of the TiO_2 nanotube via a solvothermal treatment. The $\text{SnIn}_4\text{S}_8/\text{TiO}_2$ composite exhibited better photocathodic protection performance compared with pure TiO_2 nanotubes, owing to its good visible-light response and photogenerated carrier separation efficiency. Moreover, the composite exhibited a maximum photocurrent density of $100 \mu\text{A cm}^{-2}$ for a 6 h solvothermal reaction under visible light irradiation. The negative shift of the photoinduced potential of Q235 carbon steel connected to the composite could reach 0.45 V versus SCE. Therefore, the $\text{SnIn}_4\text{S}_8/\text{TiO}_2$ composite can offer efficient photocathodic protection for Q235 carbon steel against corrosion in 3.5 wt% NaCl solution. This work provides a new approach for the development of high-efficient photoanode materials for the photocathodic protection of metals.

Keywords: TiO_2 nanotubes, SnIn_4S_8 , Carbon steel, Photocathodic protection

Introduction

With the high-speed growth of industrial technology, metal corrosion has become a global problem [1, 2]. Metal corrosion not only shortens the service life of the equipment but also causes huge economic losses, even catastrophic safety accidents and environmental problems. Specifically, Q235 carbon steel (CS) is prone to severe corrosion in NaCl solution [3]. Photocathodic protection is an environmentally friendly and cost-saving technology with great application potential for metal anti-corrosion [4], which uses clean solar energy unlike conventional anti-corrosion technology. In addition, semiconductor photoanode materials are not consumed like traditional sacrificial anodes. This technology

uses semiconductor materials (TiO_2 [5], $\text{g-C}_3\text{N}_4$ [6], ZnO [7, 8], SrTiO_3 [9]) to harvest solar photons and convert light energy into electricity to drive reduction chemical reactions efficiently, thereby effectively alleviating metal corrosion.

TiO_2 has been widely used as a photoelectrode material for photocathodic protection due to its wide application range to catalyze various redox reactions, as well as its low cost, non-toxicity, and high chemical and photochemical stability [10–12]. However, individual TiO_2 materials can only be induced by UV light as a result of their broad bandgap (3.0 eV for rutile, 3.2 eV for anatase). In addition, the available photoelectrons are reduced due to the rapid recombination of photogenerated carriers. To overcome the above disadvantages, numerous approaches have been proposed to heighten the photocathodic protection ability of TiO_2 -based photoelectrodes. These approaches include surface modification [13], designing highly ordered TiO_2 nanotubes (NTs) [14], doping with metals or non-metals [15–18], and

*Correspondence: lhqdio1987@163.com

¹ State Key Laboratory of Bio-Fibers and Eco-Textiles, College of Mechanical and Electrical Engineering, Qingdao University, No. 308 Ningxia Road, Qingdao 266071, People's Republic of China
Full list of author information is available at the end of the article

constructing heterojunctions [19–21]. More specifically, constructing heterojunctions by combining with other materials has proven to be a valid method for improving the photoelectrochemical properties of TiO_2 . The materials used for this strategy include metal oxides (In_2O_3 [22], MoO_3 [23], Bi_2O_3 [24], WO_3 [25, 26], RuO_2 [27, 28]), metal sulfides and selenides (Ag_2S [29], Bi_2S_3 [30], Ag_2Se [31]), graphene [32–34], $\text{Co}(\text{OH})_2$ [35], and ZnFeAl-layered double hydroxides [36].

In addition, ternary and quaternary chalcogenides and selenium compounds, such as $\text{Cu}_2\text{AgInS}_4$ [37], $\text{Cu}_2\text{AgInSe}_4$ [38], and $\text{Cu}_2\text{ZnSnSe}_4$ [39], have received considerable attention in recent years due to their good photostability, strong absorption in the visible light range, and good electron transport properties. These materials have shown high photocatalytic activity to improve the photoconversion efficiency of quantum dot-sensitized solar cells. Stannum indium sulfide (SnIn_4S_8) is a ternary chalcogenide semiconductor [40] that shows promising applications in heavy metal reduction and the photocatalytic degradation of organics and pharmaceutical wastewater due to its good chemical stability and strong absorption of visible light [41, 42]. The physical and chemical ability of nanomaterials is mainly determined by their size, structure, and morphology. SnIn_4S_8 nanosheets have a large specific surface area, which may facilitate visible-light absorption [43] and reduce film resistance due to the fast charge transfer between the nanosheet and the electrolyte [44]. In addition, SnIn_4S_8 nanosheets have a relatively negative conduction band, which is beneficial to providing photocathodic protection for metals with a negative self-corrosion potential. Therefore, SnIn_4S_8 nanosheet-modified TiO_2 NTs may show improved photoelectrochemical and photocathodic protection performance. However, there are only a few reports on the fabrication and cathodic protection application of SnIn_4S_8 nanosheet/ TiO_2 nanotube composites.

In the present study, a SnIn_4S_8 nanosheet/ TiO_2 NT heterojunction film was synthesized through a solvothermal reaction and subsequent electrochemical anodic oxidation method. The photocathodic protection performance and mechanism of SnIn_4S_8 / TiO_2 composites for Q235 CS were systematically studied.

Methods

Fabrication of SnIn_4S_8 / TiO_2 Photoelectrodes

TiO_2 NTs were prepared on a titanium sheet ($1\text{ cm} \times 4\text{ cm}$) by an electrochemical anodic oxidation process. The titanium sheet was cleaned after chemical polishing and anodized under 30 V for 30 min using ethylene glycol and 0.45 wt% NH_4F and 8 wt% H_2O as an electrolyte solution. A platinum sheet was used as the cathode. The sample was rinsed with deionized water and

dried at 60 °C. TiO_2 NTs were then acquired after heat treatment under 450 °C for 1.5 h.

SnIn_4S_8 / TiO_2 NTs photoelectrodes were fabricated by depositing SnIn_4S_8 nanosheets on the surface of the TiO_2 NTs through a simple solvothermal process (Fig. 1a). Typically, 0.05 mmol $\text{SnCl}_4 \cdot 5\text{H}_2\text{O}$ (0.0175 g), 0.2 mmol InCl_3 (0.0587 g), and 0.5 mmol thioacetamide (0.0375 g) were added to 80 mL of absolute ethanol and stirred until the solution was homogeneous. The above solution and titanium sheet with fabricated TiO_2 NTs were placed on the bottom of a 100 mL Teflon-lined stainless steel autoclave at 180 °C for 3–12 h. Then, the sample was cleaned repeatedly with absolute ethanol and dried at 70 °C for 4 h. The synthesized composites were marked as 3 h SnIn_4S_8 / TiO_2 , 6 h SnIn_4S_8 / TiO_2 , 9 h SnIn_4S_8 / TiO_2 , 12 h SnIn_4S_8 / TiO_2 , respectively. For comparison, SnIn_4S_8 nanosheets were prepared on the titanium sheet using the same procedure.

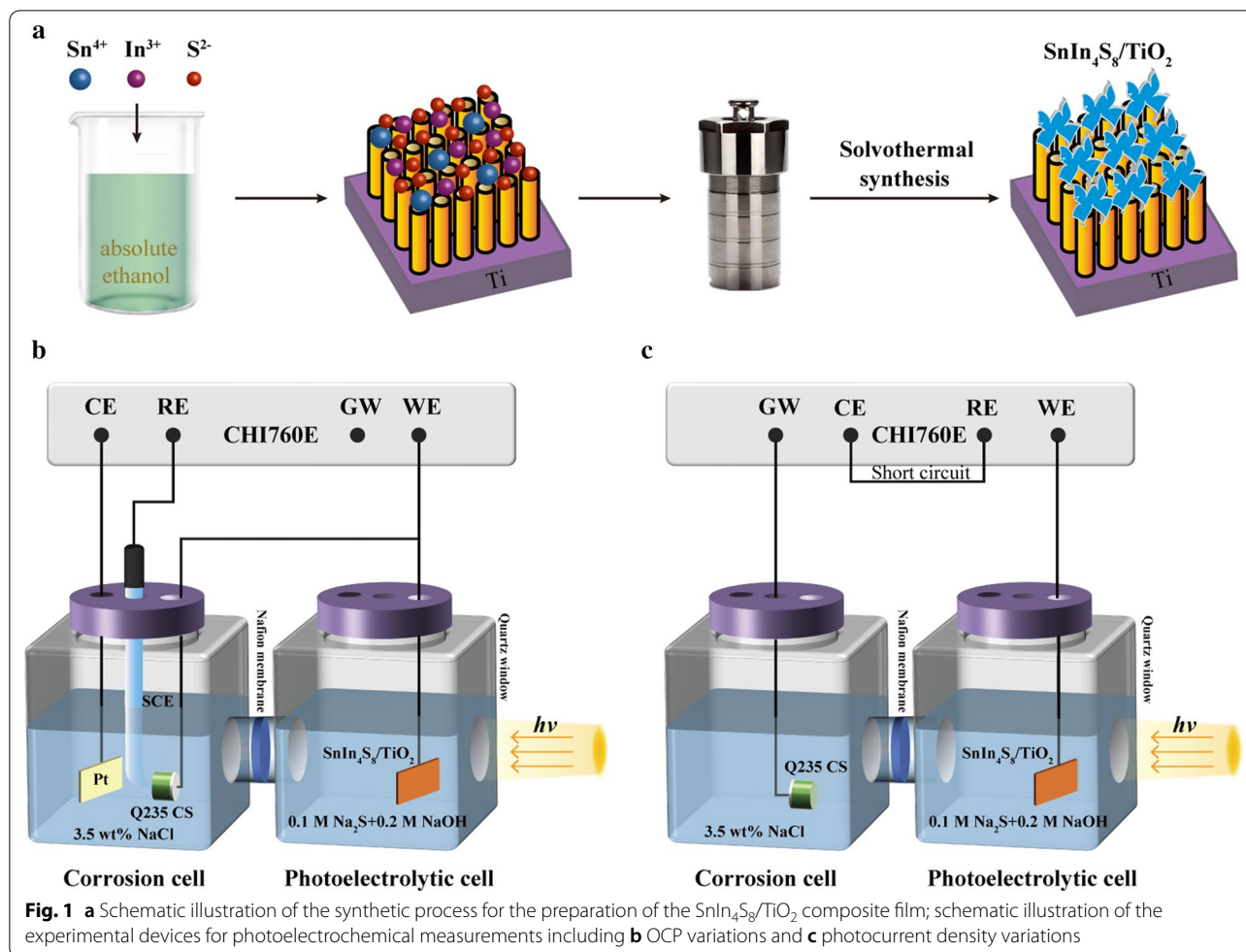
Characterization

The morphology, microstructure, and elemental composition of the fabricated photoelectrodes were studied using a Hitachi SU8220 scanning electron microscope (SEM), high-resolution transmission electron microscope (HRTEM, JEOL JEM-2010), and energy dispersive spectrometer (EDS), respectively. The crystal structures of the prepared photoelectrodes were evaluated by X-ray diffraction (XRD) (D8-advance, Bruker AXS Co.) with $\text{Cu K}\alpha$ irradiation at a wavelength of 0.15406 nm. The surface composition and chemical states were evaluated by X-ray photoelectron spectroscopy (XPS, ESCALAB 250XI, Thermo Scientific Co.) using $\text{Al K}\alpha$ radiation. The optical characteristics were analyzed using a UV–Vis diffuse reflectance spectrophotometer (Hitachi UH4150). The photoluminescence (PL) spectra of the prepared photoelectrodes were measured on an FLS980 Series fluorescence spectrometer. Fourier transform infrared (FTIR) analyses were conducted on a Varian Scimitar 1000 spectrophotometer.

Photoelectrochemical Tests

Photoelectrochemical tests were performed at room temperature on an electrochemical workstation (CHI760E, Chenhua Instrument Shanghai Co., Ltd.). The visible light source was a 300 W xenon light (PLS-SXE 300C, Perfect light Beijing Co., Ltd.) with a 420 nm cut-off filter. A Q235 CS electrode acted as the metal sample for testing, which was made via embedding a Q235 CS sample ($1\text{ cm} \times 1\text{ cm} \times 1\text{ cm}$) in an epoxy resin. The composition is as follows: 0.18% C; 0.28% Si; 0.035% S; 0.04% P; 0.55% Mn, and 98.915% Fe.

Figure 1b shows the schematic illustration of the experimental device for the measurement of the variations of



the open circuit potential (OCP) of the Q235 CS coupled to the prepared photoelectrodes. The device consists of a photoelectrolytic cell and a corrosion cell, which were connected by a Nafion membrane. The prepared photoelectrodes were placed in the photoelectrolytic cell containing 0.1 M Na_2S and 0.2 M NaOH solution, and the Q235 CS was set in the corrosion cell. The Q235 CS linked to the photoelectrodes via an external Cu wire was employed as the working electrode, while a saturated calomel electrode (SCE) and a platinum sheet were utilized as the reference electrode and the contrast electrode, respectively. The photoelectrodes were shined by visible light through a quartz window. The Tafel curves were tested from -0.25 and $+0.25$ V relative to the OCP at a sweep rate of 0.5 mV s^{-1} . The electrochemical impedance spectroscopy (EIS) spectra were tested in a frequency range from 10^5 to 10^{-2} Hz. The amplitude of the AC signal was 10 mV. Figure 1c displays the schematic illustration of the experimental device for the photocurrent density variation under intermittent visible light illumination. The photoelectrodes served as the working

electrode, and Q235 CS was linked to the ground by a Cu wire. The contrast and reference electrode were short-circuited by a thin wire.

Results and Discussion

Morphologies and Chemical Compositions

Figure 2 reveals the morphologies of the TiO_2 and $\text{SnIn}_4\text{S}_8/\text{TiO}_2$ composite films. As shown in Fig. 2a, b, a well-aligned and highly ordered NTs film was successfully formed on the titanium surface through an electrochemical anodic oxidation process. The average inner diameter of TiO_2 NTs was approximately 50 nm, the wall thickness was approximately 25 nm, and the tube length was approximately 1300 nm. It can be observed that numerous curved SnIn_4S_8 nanosheets were attached to the TiO_2 surface after a solvothermal reaction for 6 h (Fig. 2c, d). The nanostructure composed of thin nanosheets and large hierarchical pores was conducive to the improvement of the light harvestability due to multiple light scattering, which may facilitate the charge transfer in the

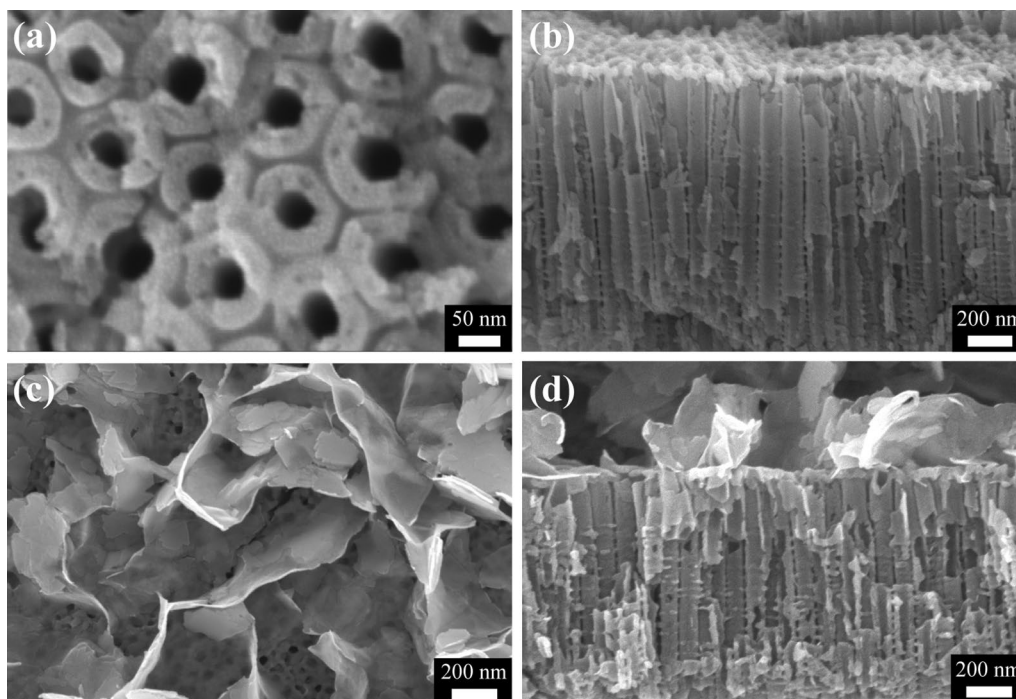


Fig. 2 **a** Topographic and **b** cross-sectional SEM images of the TiO_2 NT films, **c** topographic and **d** cross-sectional SEM images of the $\text{SnIn}_4\text{S}_8/\text{TiO}_2$ composite film

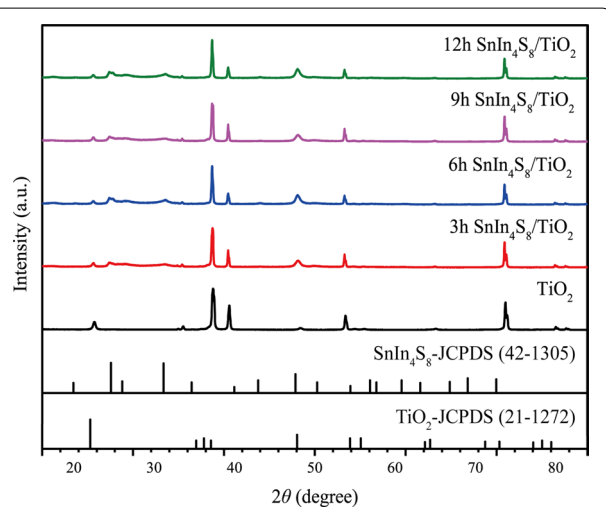


Fig. 3 XRD spectra of pure TiO_2 and the different $\text{SnIn}_4\text{S}_8/\text{TiO}_2$ composites

photochemical reaction and enhance the photocathodic protection performance of the $\text{SnIn}_4\text{S}_8/\text{TiO}_2$ composite.

Figure 3 shows the XRD spectra of the synthesized TiO_2 and the $\text{SnIn}_4\text{S}_8/\text{TiO}_2$ composite films. For pure TiO_2 , except for the characteristic peaks of the titanium substrate, the peaks at 25.3° , 48.1° , and 53.9° were indexed

to the anatase (101), (200), and (105) lattice planes, respectively (JCPDS Card No. 21-1272). For the $\text{SnIn}_4\text{S}_8/\text{TiO}_2$ composites, the XRD patterns of the obtained samples were similar. Compared with pure TiO_2 , three other diffraction peaks were observed in the XRD spectra of the $\text{SnIn}_4\text{S}_8/\text{TiO}_2$ composites. The peaks at 27.5° , 28.4° , and 33.0° were assigned to the lattice planes (311), (222), and (400) of tetragonal SnIn_4S_8 , respectively (JCPDS Card No. 42-1305). No peaks corresponding to binary sulfides and oxides were detected, confirming the high purity of the $\text{SnIn}_4\text{S}_8/\text{TiO}_2$ composites.

To further study the microstructures of the $\text{SnIn}_4\text{S}_8/\text{TiO}_2$ composite, TEM images were analyzed as shown in Fig. 4a, b, confirming that the SnIn_4S_8 nanosheets were attached to the TiO_2 NTs surface. The wall thickness and inner diameter of the TiO_2 NTs were approximately 25 and 50 nm, respectively, which was consistent with the SEM results. Figure 4c is an HRTEM image taken at the edge of the surface of the composite in Fig. 4a, which displays a close contact between the TiO_2 NTs and the SnIn_4S_8 nanosheets. The lattice fringe with a spacing of 0.358 nm was assigned to the anatase (101) plane of TiO_2 (JCPDS Card No. 21-1272). The lattice fringe with a spacing of 0.268 nm and 0.323 nm was indexed to the tetragonal (400) and (311) planes of SnIn_4S_8 (JCPDS Card No. 42-1305), respectively. The results confirmed that

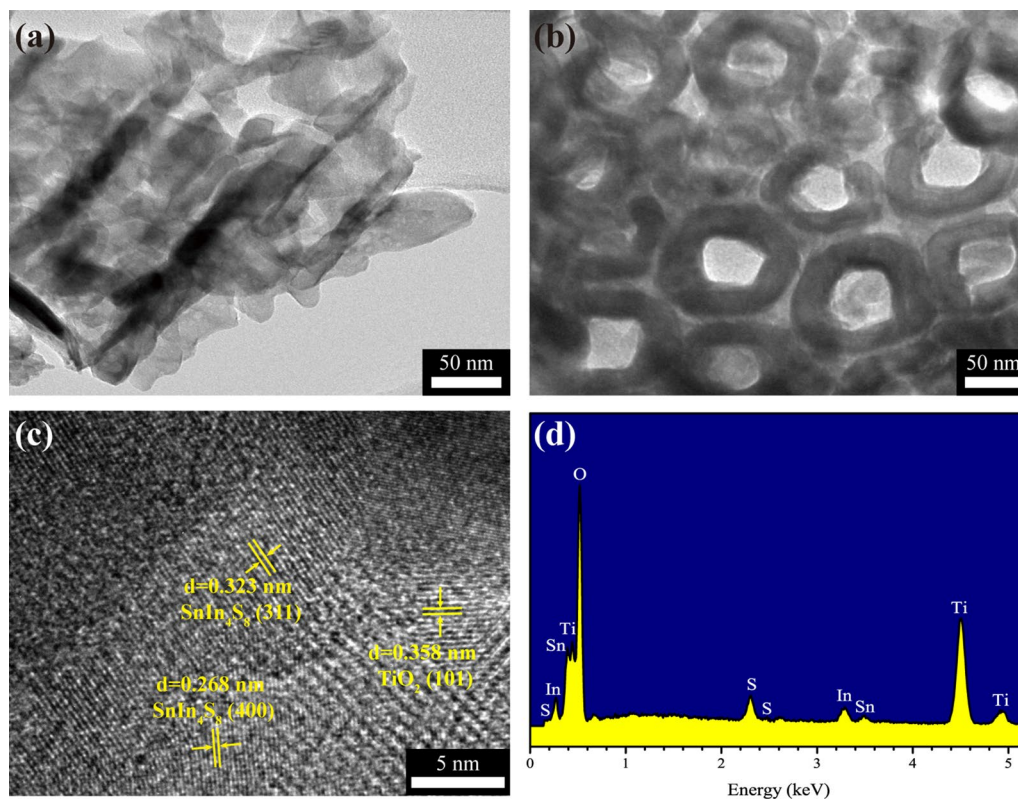


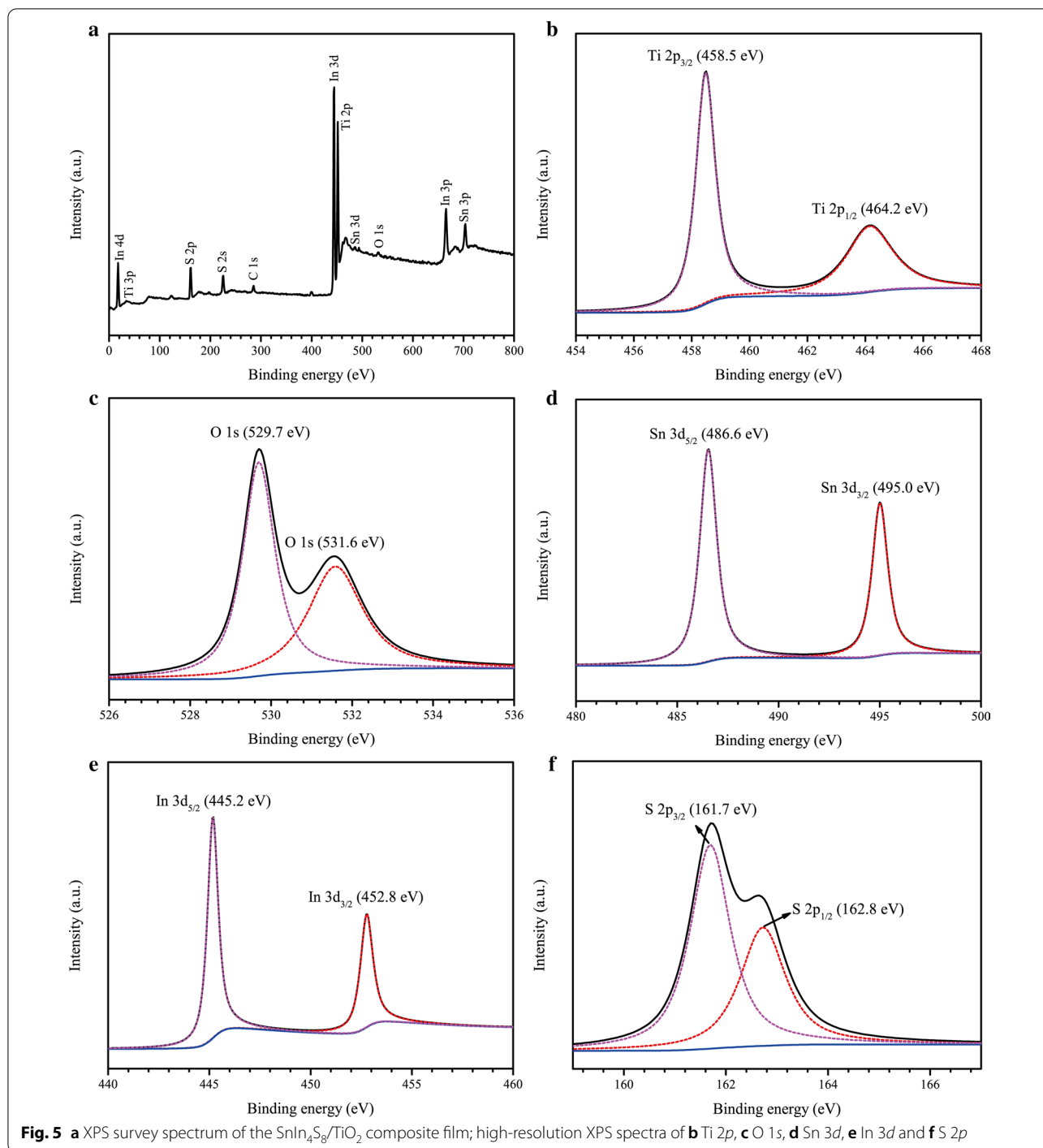
Fig. 4 a, b TEM, and c HRTEM images, and d EDS spectrum of the $\text{SnIn}_4\text{S}_8/\text{TiO}_2$ composite film

SnIn_4S_8 nanosheets were constructed on the TiO_2 NTs surface by the solvothermal process. The corresponding EDS spectrum (Fig. 4d) demonstrated that the $\text{SnIn}_4\text{S}_8/\text{TiO}_2$ composite film was composed of Ti, O, Sn, S, and In elements.

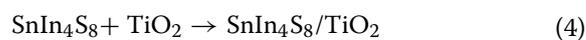
The surface components and chemical states of $\text{SnIn}_4\text{S}_8/\text{TiO}_2$ were studied by XPS. From the XPS survey spectrum (Fig. 5a), it was confirmed that Ti, O, Sn, In, S elements were present in the composite, which was consistent with the EDS result. Moreover, a characteristic peak corresponding to the C element was observed, which was caused by exposure to atmospheric pollution. Figure 5b displays the high-resolution XPS spectrum of Ti 2p. The peaks of the binding energy at 458.5 and 464.2 eV were coincident with Ti 2p_{3/2} and Ti 2p_{1/2}, respectively, which are characteristic peaks of Ti⁴⁺ [45]. This indicated that Ti⁴⁺ existed in the $\text{SnIn}_4\text{S}_8/\text{TiO}_2$ composite. Figure 5c shows the peaks at 529.7 and 531.6 eV, which correspond to lattice oxygen and adsorbed oxygen, respectively [46]. The lattice oxygen represented the Ti–O, indicating the existence of TiO_2 in the composite. The adsorbed oxygen came from H₂O adsorbed on the surface of the composite, suggesting that the surface of the composite was rich in oxygen vacancies. Figure 5d

reveals that the peak centered at 495.0 and 486.6 eV belonged to Sn 3d_{3/2} and Sn 3d_{5/2}, respectively [40], indicating that the valence state of Sn was +4. As shown in Fig. 5e, the binding energies of 445.2 and 452.8 eV were assigned to In 3d_{5/2} and In 3d_{3/2}, respectively, suggesting the existence of In³⁺ in the composite [47]. The peaks at 162.8 and 161.7 eV in Fig. 5f correspond to S 2p_{1/2} and S 2p_{3/2}, respectively, showing that S element existed mainly in the form of S²⁻ in the $\text{SnIn}_4\text{S}_8/\text{TiO}_2$ NTs [48]. The above results further indicate that a $\text{SnIn}_4\text{S}_8/\text{TiO}_2$ NTs heterojunction film was successfully synthesized by the combination of a solvothermal and electrochemical anodic oxidation process, which was in good agreement with the results from SEM, TEM, and XRD analyzes.

To investigate the growth process of the SnIn_4S_8 nanosheets, the SEM images of the composites fabricated by the solvothermal process for 3, 9, and 12 h were observed. When the reaction time was 3 h, small SnIn_4S_8 nanosheets appeared on the surface of the TiO_2 NTs in the obtained composite (Additional file 1: Fig. S1a, d). After the time reached 6 h, the size and thickness of the nanosheets increased (Fig. 2c, d). However, once the solvothermal reaction time exceeded 9 h, the SnIn_4S_8 nanosheets completely covered the TiO_2 surface and



blocked the mouth of the TiO₂ NTs, which was harmful to the photogenerated charge separation (Additional file 1: Fig. S1b, c, e, f). The main reactions during the fabrication process are as follows:



Optical Characteristics

The optical characteristics of the fabricated photoelectrodes were analyzed by UV–visible diffuse reflectance spectra (Fig. 6a). The light absorption of pure TiO_2 was mainly in the UV region, and the absorption edge was approximately 385 nm, which was attributed to the inherent absorption of TiO_2 . Moreover, the light absorption of TiO_2 in the visible region may be ascribed to light scattering caused by cracks or holes in the NTs [49]. The absorption edge of SnIn_4S_8 and the $\text{SnIn}_4\text{S}_8/\text{TiO}_2$ composite appeared near 590 and 535 nm, respectively. The bandgap (E_g) values of the photoelectrodes were computed using the following equation [50]:

$$(\alpha h\nu)^2 = A(h\nu - E_g) \quad (5)$$

where α , $h\nu$, and A imply the absorption coefficient, photon energy, and characteristic constant, respectively. The plot of $(\alpha h\nu)^2$ versus $h\nu$ for calculating the bandgap is displayed in Fig. 6b. The E_g value of pure TiO_2 was 3.22 eV, which was similar to that of anatase TiO_2 (3.2 eV) [51]. The E_g value of SnIn_4S_8 and the $\text{SnIn}_4\text{S}_8/\text{TiO}_2$ composite was evaluated to be 2.1 and 2.32 eV, respectively. These results indicated that the absorption capacity of the $\text{SnIn}_4\text{S}_8/\text{TiO}_2$ composite was enhanced in the visible light region, which is beneficial to the utilization of solar energy and improvement of the photocathodic protection performance.

The PL spectra measurement was used to examine the separation, transfer, and recombination of photogenerated carriers of semiconductor materials [52]. The weaker PL intensity means the lower the recombination rate of photogenerated carriers [53]. The PL intensity of the $\text{SnIn}_4\text{S}_8/\text{TiO}_2$ composite was lower than that of TiO_2 NTs (Additional file 1: Fig. S2), indicating that the sensitization of the SnIn_4S_8 nanosheets could effectively

restrain the recombination of photogenerated carriers in the TiO_2 NTs.

Photoelectrochemical Performance

Photocurrent density is a significant parameter used to investigate the photocathodic protection properties of semiconductor photoanodes. The greater the photocurrent density of the metal coupled to the photoanode, the better the photoelectric conversion performance and the photocathodic protection effect of the photoanode [54]. Figure 7a displays the photocurrent density changes of a Q235 CS electrode coupled to pure TiO_2 or $\text{SnIn}_4\text{S}_8/\text{TiO}_2$ NTs photoanodes. Before the lamp was turned on, the photocurrent densities of the metal electrode coupled to the photoanodes were almost zero, indicating no photogenerated electrons were transferred to the steel electrode at this time. When the light was turned on, both pure TiO_2 and the $\text{SnIn}_4\text{S}_8/\text{TiO}_2$ composite photoanodes exhibited a photocathodic protection current for the Q235 CS electrode. This was because photogenerated electrons were carried from the photoanodes to the surface of the steel electrode. The $\text{SnIn}_4\text{S}_8/\text{TiO}_2$ composite fabricated by the 6 h solvothermal reaction demonstrated the greatest photocurrent density (about $100 \mu\text{A cm}^{-2}$), which was approximately 8 times larger than pure TiO_2 . This indicates that the modification of the SnIn_4S_8 nanosheets remarkably enhanced the photoelectron separation and transmission efficiency of the TiO_2 NTs. The photocurrent densities decreased in the order of 6 h $\text{SnIn}_4\text{S}_8/\text{TiO}_2 > 9 \text{ h SnIn}_4\text{S}_8/\text{TiO}_2 > 12 \text{ h SnIn}_4\text{S}_8/\text{TiO}_2 > 3 \text{ h SnIn}_4\text{S}_8/\text{TiO}_2 > \text{TiO}_2$. As the time of the solvothermal reaction increased, the SnIn_4S_8 nanosheets absorbed more light energy to generate sufficient photoelectrons, thus exhibiting a larger photocurrent. However, when the solvothermal reaction time exceeded 6 h, the increase in

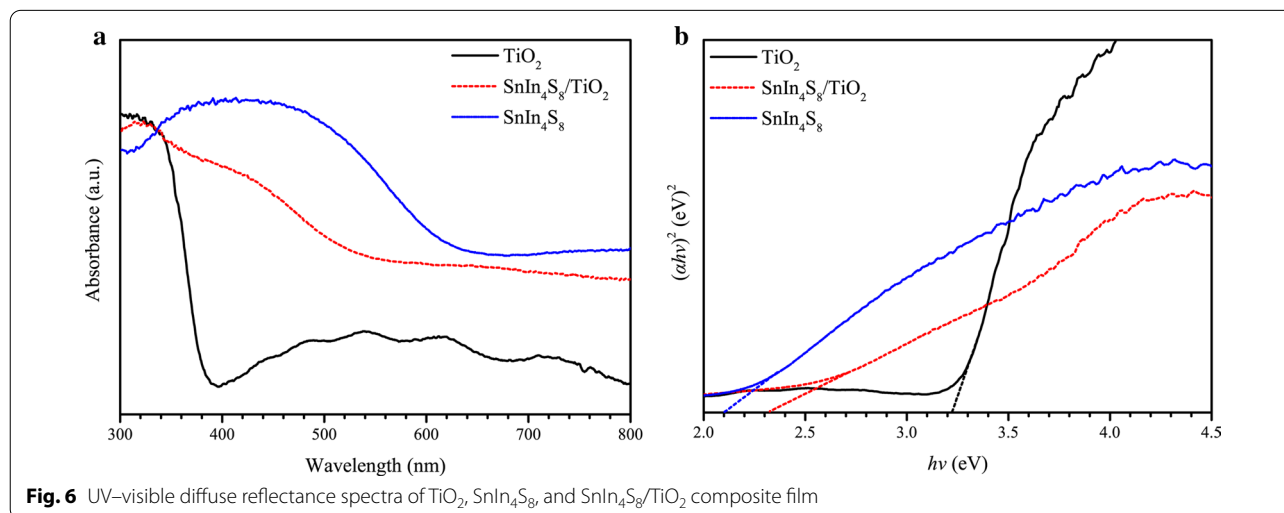
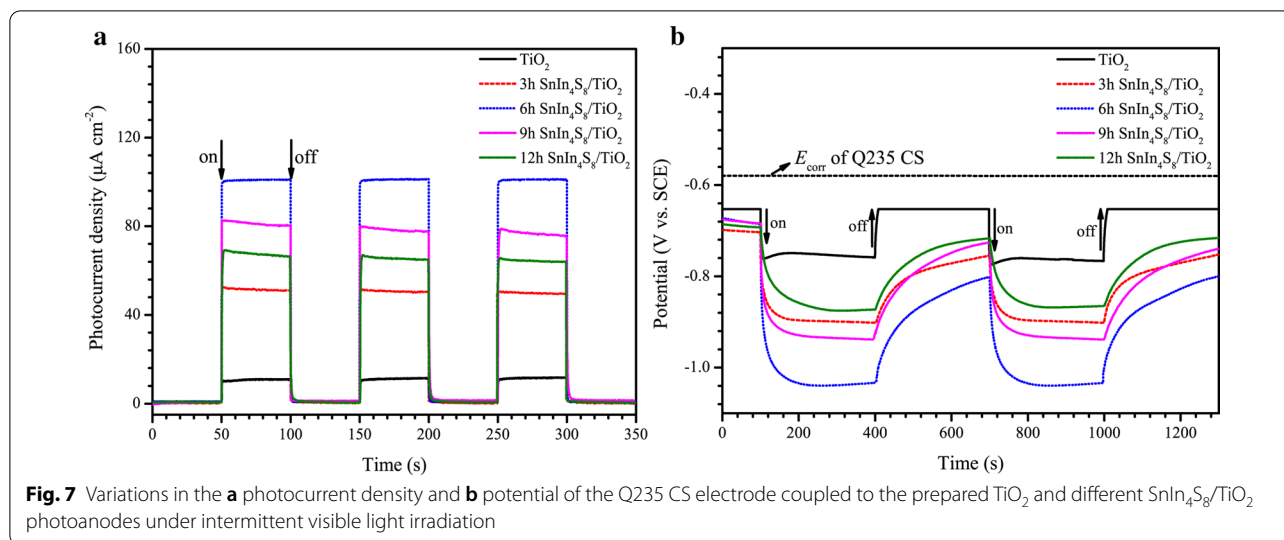


Fig. 6 UV–visible diffuse reflectance spectra of TiO_2 , SnIn_4S_8 , and $\text{SnIn}_4\text{S}_8/\text{TiO}_2$ composite film



the thickness of the nanosheets increased the transfer distance of the photoelectrons in the nanosheets [55, 56]. In addition, the TiO_2 NTs cannot absorb light to generate photoelectrons since the oversized SnIn_4S_8 nanosheets blocked their mouth. This ultimately led to a decrease in photoelectrons transferred to the Ti substrate, which decreased the photocurrent of the composite.

The variation of the potential of the metal coupled to the semiconductor photoanode is another considerable parameter used to investigate the photocathodic protection property of the photoanodes [57]. Photo-excitation of the photoanodes generates electrons, which are transferred to the surface of the steel and reduce its potential, and then protect the steel electrode. Figure 7b demonstrates the OCP changes of Q235 CS linked to TiO_2 and $\text{SnIn}_4\text{S}_8/\text{TiO}_2$ NTs photoanodes. The potentials of the coupled Q235 CS decreased slightly before illumination due to the galvanic effect. After the light was turned on, the photogenerated potentials of the Q235 CS electrode coupled to TiO_2 and $\text{SnIn}_4\text{S}_8/\text{TiO}_2$ NTs had undergone significant negative shifts. The order of the potential drop was 6 h $\text{SnIn}_4\text{S}_8/\text{TiO}_2$ (0.45 V vs. SCE) > 9 h $\text{SnIn}_4\text{S}_8/\text{TiO}_2$ (0.36 V vs. SCE) > 3 h $\text{SnIn}_4\text{S}_8/\text{TiO}_2$ (0.32 V vs. SCE) > 12 h $\text{SnIn}_4\text{S}_8/\text{TiO}_2$ (0.30 V vs. SCE) > TiO_2 (0.18 V vs. SCE). The potentials of Q235 CS linked to the $\text{SnIn}_4\text{S}_8/\text{TiO}_2$ composites slowly increased after the light was turned off, and the coupled potentials were still much lower than that of bare Q235 CS. This indicated that the composites could continue to protect the steel for some time even in the absence of light due to the slow release of electrons stored in the composites. Therefore, combined with the results of photocurrent densities, it can be concluded that the $\text{SnIn}_4\text{S}_8/\text{TiO}_2$ composites had better photocathodic protection for Q235 CS than pure TiO_2 . The

optimal photocathodic protection was achieved for the $\text{SnIn}_4\text{S}_8/\text{TiO}_2$ composite prepared for 6 h. In addition, the 6 h $\text{SnIn}_4\text{S}_8/\text{TiO}_2$ composite photoanode displayed higher photocathodic protection properties than most photoanodes previously reported (Additional file 1: Table S1). The $\text{SnIn}_4\text{S}_8/\text{TiO}_2$ composites mentioned in the following sections were obtained for the sample developed by 6 h of reaction time.

In order to investigate the stability of the $\text{SnIn}_4\text{S}_8/\text{TiO}_2$ composite, the long term potential variation of a Q235 CS electrode connected to the photoanode under intermittent visible light illumination was analyzed. As displayed in Fig. 8a, the self-corrosion potential of the bare Q235 CS was -0.58 V versus SCE in 3.5 wt % NaCl solution. When the CS was connected to the $\text{SnIn}_4\text{S}_8/\text{TiO}_2$ composite, the potential dropped rapidly with visible light irradiation, which may be due to the transfer of photogenerated electrons from the composite to the steel. Under long term visible light irradiation, the potential of steel was stable at -0.96 V versus SCE. This was only 0.07 V higher than the photogenerated potential obtained from the OCP results, indicating that the $\text{SnIn}_4\text{S}_8/\text{TiO}_2$ composite had good stability. After the light irradiation was stopped, the potential of Q235 CS increased back to -0.74 V versus SCE, which was still far from the self-corrosion potential, demonstrating that the composite can provide the steel with continuous protection in the dark state. Moreover, as shown in Fig. 8b, c, the XRD pattern and FTIR spectrum of the $\text{SnIn}_4\text{S}_8/\text{TiO}_2$ composite after the photoelectrochemical test were consistent with those before the test, respectively, indicating that the composite possesses good photoelectrochemical stability.

The Tafel curves of the pure Q235 CS, the Q235 CS electrode linked to the pure TiO_2 , and the 6 h $\text{SnIn}_4\text{S}_8/$

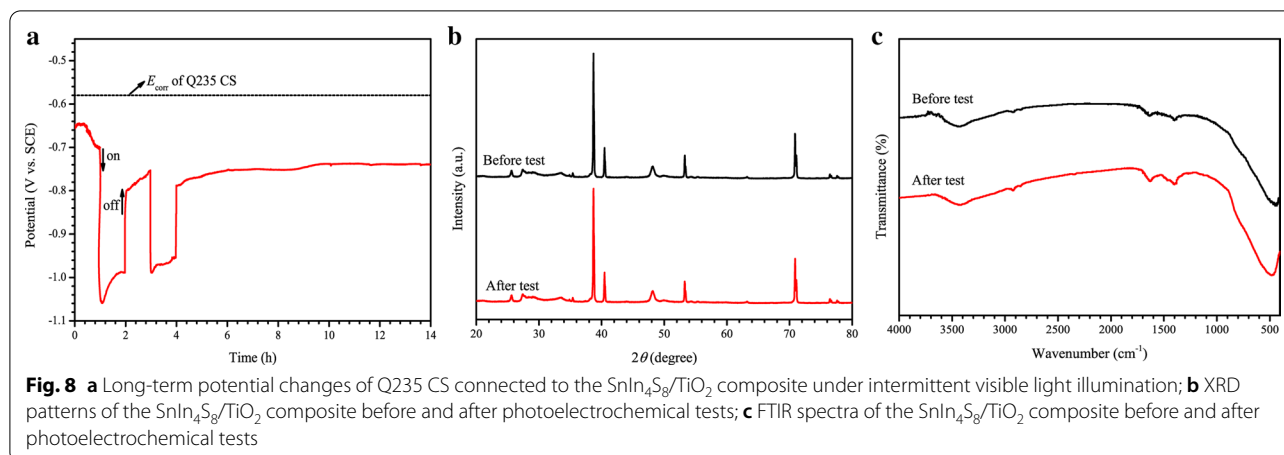


Fig. 8 **a** Long-term potential changes of Q235 CS connected to the $\text{SnIn}_4\text{S}_8/\text{TiO}_2$ composite under intermittent visible light illumination; **b** XRD patterns of the $\text{SnIn}_4\text{S}_8/\text{TiO}_2$ composite before and after photoelectrochemical tests; **c** FTIR spectra of the $\text{SnIn}_4\text{S}_8/\text{TiO}_2$ composite before and after photoelectrochemical tests

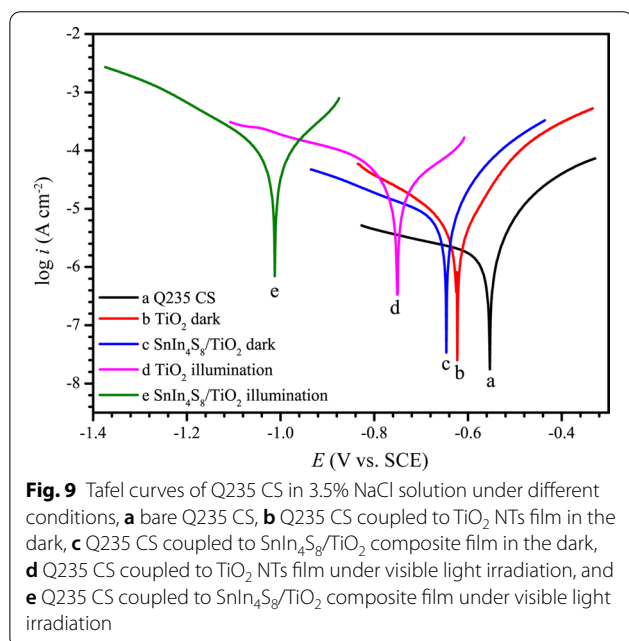


Fig. 9 Tafel curves of Q235 CS in 3.5% NaCl solution under different conditions, **a** bare Q235 CS, **b** Q235 CS coupled to TiO_2 NTs film in the dark, **c** Q235 CS coupled to $\text{SnIn}_4\text{S}_8/\text{TiO}_2$ composite film in the dark, **d** Q235 CS coupled to TiO_2 NTs film under visible light irradiation, and **e** Q235 CS coupled to $\text{SnIn}_4\text{S}_8/\text{TiO}_2$ composite film under visible light irradiation

TiO_2 composite in dark conditions and under irradiation were tested to further evaluate the photoelectrochemical performance of the $\text{SnIn}_4\text{S}_8/\text{TiO}_2$ composites (Fig. 9). Corrview software was utilized to compute the corrosion potential (E_{corr}) and corrosion current (i_{corr}), and the results are displayed in Table 1. Under visible light irradiation, after Q235 CS was linked to the pure TiO_2 or the $\text{SnIn}_4\text{S}_8/\text{TiO}_2$ composite electrode, the E_{corr} shifted negatively, indicating that photogenerated electrons effectively migrated from the photoelectrode to the steel electrode, thereby providing a photocathodic protection effect for the Q235 CS electrode. The E_{corr} of Q235 CS linked to the $\text{SnIn}_4\text{S}_8/\text{TiO}_2$ composite (-0.92 V vs. SCE) under irradiation was much lower than that of pure TiO_2

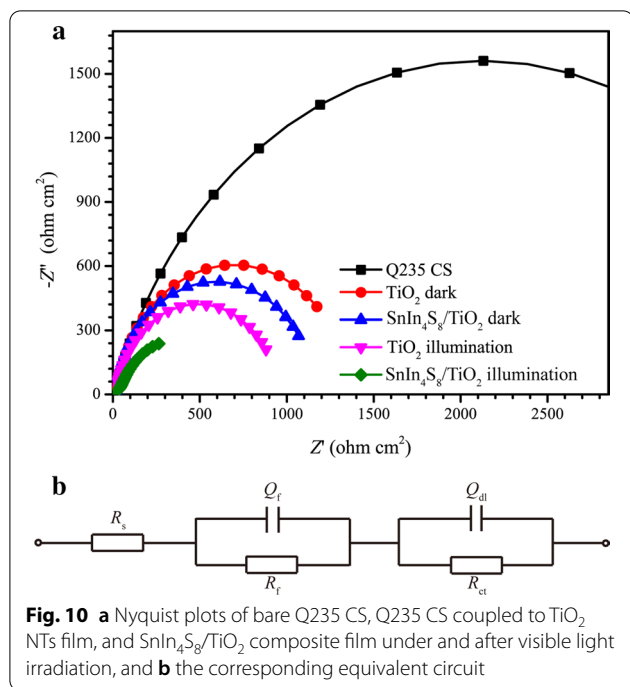
Table 1 Electrochemical parameters obtained by the Tafel curves of Q235 CS, TiO_2 in the dark, $\text{SnIn}_4\text{S}_8/\text{TiO}_2$ in the dark, TiO_2 under illumination, and $\text{SnIn}_4\text{S}_8/\text{TiO}_2$ under illumination

Samples	E_{corr} (V vs. SCE)	i_{corr} ($\mu\text{A cm}^{-2}$)
Q235 CS	-0.554	1.658
TiO_2 dark	-0.623	3.144
$\text{SnIn}_4\text{S}_8/\text{TiO}_2$ dark	-0.646	5.313
TiO_2 illumination	-0.751	18.94
$\text{SnIn}_4\text{S}_8/\text{TiO}_2$ illumination	-1.011	63.10

(-0.75 V vs. SCE), showing that the composite was able to provide Q235 CS with better cathodic protection than pure TiO_2 . The i_{corr} of Q235 CS linked to the $\text{SnIn}_4\text{S}_8/\text{TiO}_2$ composite notably increased compared with that of bare Q235 CS under light irradiation (Table 1). This is as a result of the polarization of photoinduced electrons accelerating the rate of chemical reactions at the interface [58, 59].

EIS was used to further study the photogenerated carrier separation and transfer process of the $\text{SnIn}_4\text{S}_8/\text{TiO}_2$ composite film and the corrosion resistance of the Q235 CS electrode. Figure 10a shows the Nyquist plots of Q235 CS, Q235 CS coupled to a TiO_2 NT film, and the $\text{SnIn}_4\text{S}_8/\text{TiO}_2$ composite film under and after visible light irradiation. The fitting circuit for EIS using ZSimpWin software consisted of an $R_s(Q_f R_f)(Q_{dl} R_{ct})$ model, as demonstrated in Fig. 10b, where R_s indicates the electrolyte resistance, Q_f and R_f indicate the capacitance and resistance of the semiconductor film electrode at high frequencies, respectively, and Q_{dl} and R_{ct} indicate the electric double-layer capacitance and the charge transfer resistance at low frequencies, respectively.

The fitting impedance parameters of EIS using the equivalent circuit are also shown in Table 2. The diameter



of the impedance arc of the coupled Q235 CS electrode under visible light was smaller than that of pure Q235 CS, and the R_{ct} values of the coupled Q235 CS electrode decreased significantly. The results indicate that the rate of the electrochemical reaction at the interface between the Q235 CS and the solution increased remarkably, which may be due to the migration of photoelectrons from the photoanode to the Q235 CS [60]. In addition, the R_{ct} value of the SnIn₄S₈/TiO₂ composite was smaller than that of TiO₂, which may be because the heterojunction formed by TiO₂ and SnIn₄S₈ was conducive to the separation and migration of photoinduced charges. These results were consistent with those obtained from the Tafel curves (Fig. 9). Furthermore, the diameter of the impedance arc of the SnIn₄S₈/TiO₂ composite under visible light was distinctly smaller than the impedance after the light was turned off, suggesting that more photoelectrons migrated from the SnIn₄S₈/TiO₂ composite

to Q235 CS under visible light irradiation. This demonstrates that the SnIn₄S₈/TiO₂ composite could offer Q235 CS effective photocathodic protection in the presence of visible light.

Mechanism

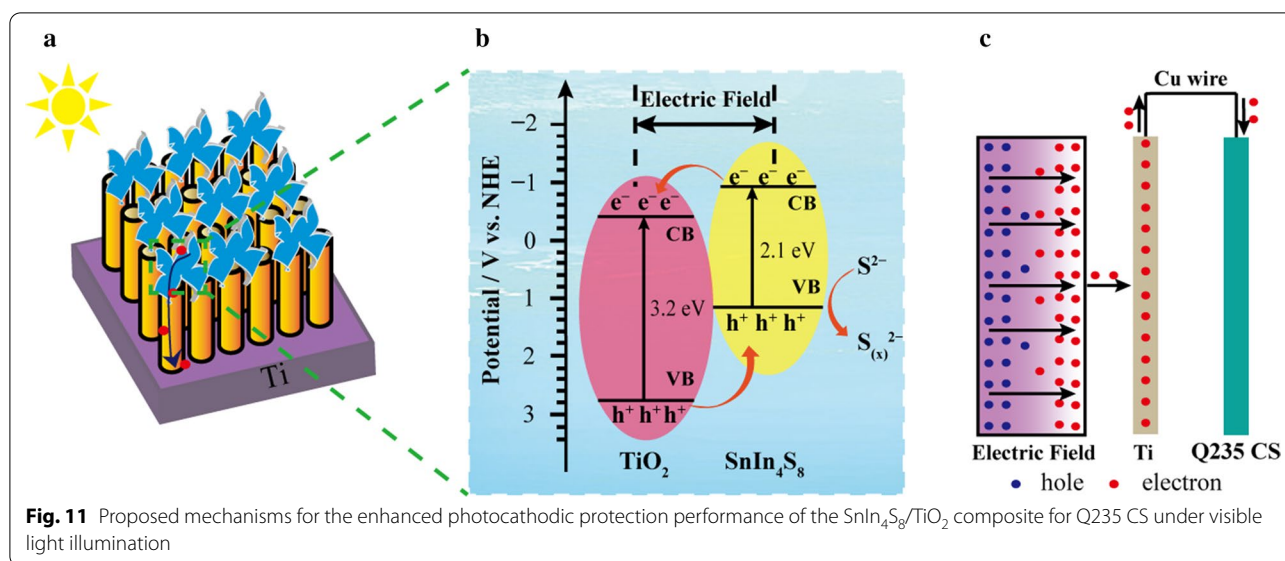
Figure 11 displays the proposed mechanism for the above-mentioned photocathodic protection of the SnIn₄S₈/TiO₂ composites and the photoelectron separation and transfer process. When the visible light illuminated the SnIn₄S₈/TiO₂ heterojunction, both the SnIn₄S₈ and TiO₂ were excited to generate photoelectrons and holes. The photoelectrons migrated from the conduction band of SnIn₄S₈ to the conduction band of TiO₂ because the potential of the former is much lower than that of TiO₂ (Fig. 11a, b). Subsequently, these electrons migrated to the surface of the steel electrode driven by the electric field force because the potential was lower than its self-corrosion potential (Fig. 11c). This process inhibited the corrosion of the Q235 CS as a result of cathodic polarization. Meanwhile, the photogenerated holes moved from the valence band of TiO₂ to the valence band of SnIn₄S₈. After the light was turned off, the stored electrons in the SnIn₄S₈/TiO₂ composites migrated continually to the Q235 CS electrode, which realized the protection of steel in the dark state. In addition, the photogenerated holes reacted with S²⁻ in the electrolyte solution to form polysulfides (S_(x)²⁻) [61], which could accelerate the photogenerated carrier separation.

Conclusions

With the increasingly prominent energy crisis and environmental pollution caused by metal corrosion, there is an urgent need to develop highly efficient visible-light-responsive semiconductor photoanodes. In this study, a SnIn₄S₈/TiO₂ nanotube photoanode was successfully fabricated via a solvothermal treatment and subsequent electrochemical anodic oxidation method. The results indicated that the nanostructure of the SnIn₄S₈/TiO₂ composite consisted of thin nanosheets and large hierarchical pores, which were conducive to photogenerated carrier separation. The optical characteristic analysis

Table 2 Fitting impedance parameters of Nyquist plots using the equivalent circuit in Fig. 10b

Samples	R_s (Ω cm ²)	Q_f		R_f (Ω cm ²)	Q_{dl}		R_{ct} (k Ω cm ²)
		$10^3 Y_{01} (S^n \cdot \Omega^{-1} \text{ cm}^{-2})$	n_1		$10^3 Y_{02} (S^n \cdot \Omega^{-1} \text{ cm}^{-2})$	n_2	
Q235 CS	5.875	1.918	0.825	6.617	1.185	0.809	4.238
TiO ₂ ^{dark}	5.220	1.603	0.813	20.84	3.080	0.934	1.343
SnIn ₄ S ₈ /TiO ₂ ^{dark}	5.182	3.235	0.885	19.31	3.042	0.936	1.141
TiO ₂ ^{illumination}	4.993	2.257	0.922	18.55	1.882	0.949	0.932
SnIn ₄ S ₈ /TiO ₂ ^{illumination}	5.343	6.283	0.873	36.47	1.947	0.825	0.278



showed that the absorption capacity of the $\text{SnIn}_4\text{S}_8/\text{TiO}_2$ composite was enhanced in the visible light region. The composite fabricated by a solvothermal reaction for 6 h exhibited the optimal photocathodic protection performance. The photocurrent density of Q235 CS coupled with the 6 h $\text{SnIn}_4\text{S}_8/\text{TiO}_2$ composite achieved $100 \mu\text{A cm}^{-2}$, which was approximately 8 times larger than pure TiO_2 . The maximum negative shift value of the photoinduced potential of Q235 CS could reach 0.45 V versus SCE. The excellent photocathodic protection effect of the $\text{SnIn}_4\text{S}_8/\text{TiO}_2$ composite for Q235 CS suggests that the composite is a promising photoelectrode material for the photocathodic protection of metals.

Supplementary information

Supplementary information accompanies this paper at <https://doi.org/10.1186/s11671-020-03447-1>.

Additional file 1 Fig. S1. SEM images of the SnIn_4S_8 nanosheet/ TiO_2 composite films synthesized at 180°C for (a), (d) 3 h, (b), (e) 9 h and (c), (f) 12 h. **Fig. S2.** PL spectra of TiO_2 NTs and $\text{SnIn}_4\text{S}_8/\text{TiO}_2$ composite. **Table S1.** Comparison of previously reported catalysts for photocathodic protection.

Abbreviations

CS: Carbon steel; NTs: Nanotubes; SnIn_4S_8 : Stannum indium sulfide; SEM: Scanning electron microscope; HRTEM: High-resolution transmission electron microscope; EDS: Energy dispersive spectrometer; XRD: X-ray diffraction; XPS: X-ray photoelectron spectroscopy; PL: Photoluminescence; FTIR: Fourier transform infrared; OCP: Open circuit potential; SCE: Saturated calomel electrode; EIS: Electrochemical impedance spectroscopy; E_g : Bandgap; E_{corr} : Corrosion potential; i_{corr} : Corrosion current.

Acknowledgements

The authors would like to thank all the reviewers who participated in the review and Mjeditor (www.Mjeditor.com) for its linguistic assistance during the preparation of this manuscript.

Authors' contributions

HL performed the synthesis and characterization of $\text{SnIn}_4\text{S}_8/\text{TiO}_2$ films. WZS, XQC and YHL took part in the synthesis. BRH and LJC participated in the characterization. HL supervised the conceptual framework and drafted the manuscript. PFZ was participant in writing the manuscript. All authors read and approved the final manuscript.

Funding

This work was supported by National Natural Science Foundation of China (Grant No. 51801109), Key Research and Development Public Welfare Program of Shandong Province (Grant No. 2019GGX102086), Taishan Scholars Construction Engineering of Shandong Province (Grant No. 201511029), and Science and Technology Support Plan for Youth Innovation of Colleges in Shandong Province (Grant No. DC200000891).

Availability of data and materials

All datasets are presented in the main paper.

Competing interests

The authors declare that they have no competing interests.

Author details

¹ State Key Laboratory of Bio-Fibers and Eco-Textiles, College of Mechanical and Electrical Engineering, Qingdao University, No. 308 Ningxia Road, Qingdao 266071, People's Republic of China. ² Institute of Oceanology, Chinese Academy of Sciences, No. 7 Nanhai Road, Qingdao 266071, People's Republic of China. ³ Open Studio for Marine Corrosion and Protection, Pilot National Laboratory for Marine Science and Technology, No. 1 Wenhai Road, Qingdao 266200, People's Republic of China.

Received: 15 August 2020 Accepted: 9 November 2020
Published online: 12 January 2021

References

- Xu JB, Cao YQ, Fang L, Hu JM (2018) A one-step preparation of inhibitor-loaded silica nanocontainers for self-healing coatings. *Corros Sci* 140:349–362
- Ye YW, Zou YJ, Jiang ZL, Yang QM, Chen LY, Guo SD, Chen H (2020) An effective corrosion inhibitor of N doped carbon dots for Q235 steel in 1 M HCl solution. *J Alloys Compd* 815:152338–152347

3. Yang DP, Ye YM, Su Y, Liu S, Gong DR, Zhao HC (2019) Functionalization of citric acid-based carbon dots by imidazole toward novel green corrosion inhibitor for carbon steel. *J Clean Prod* 229:180–192
4. Bu YY, Ao JP (2017) A review on photoelectrochemical cathodic protection semiconductor thin films for metals. *Green Energy Environ* 2:331–362
5. Yuan JN, Tsujikawa S (1995) Characterization of sol-gel-derived TiO₂ coatings and their photoeffects on copper substrates. *J Electrochem Soc* 142:3444–3450
6. Bu YY, Chen ZY, Yu JQ, Li WB (2013) A novel application of g-C₃N₄ thin film in photoelectrochemical anticorrosion. *Electrochim Acta* 88:294–300
7. Sun MM, Chen ZY, Bu YY, Yu JQ, Hou BR (2014) Effect of ZnO on the corrosion of zinc, Q235 carbon steel and 304 stainless steel under white light illumination. *Corros Sci* 82:77–84
8. Yang Y, Cheng YF (2018) One-step facile preparation of ZnO nanorods as high-performance photoanodes for photoelectrochemical cathodic protection. *Electrochim Acta* 276:311–318
9. Yang Y, Cheng YF (2017) Factors affecting the performance and applicability of SrTiO₃ photoelectrodes for photoinduced cathodic protection. *J Electrochem Soc* 164:C1067–C1075
10. Zhu YF, Du RG, Li J, Qi HQ, Lin CJ (2010) Photogenerated cathodic protection properties of a TiO₂ nanowire film prepared by a hydrothermal method. *Acta Phys-Chim Sin* 26:2349–2353
11. Lei CX, Zhou H, Wang C, Feng ZD (2013) Self-assembly of ordered mesoporous TiO₂ thin films as photoanodes for cathodic protection of stainless steel. *Electrochim Acta* 87:245–249
12. Sahnesarayi MK, Sarpoolaky H, Rastegari S (2014) Effect of heat treatment temperature on the performance of nano-TiO₂ coating in protecting 316L stainless steel against corrosion under UV illumination and dark conditions. *Surf Coat Technol* 258:861–870
13. Zhang TT, Liu YP, Liang J, Wang DA (2017) Enhancement of photoelectrochemical and photocathodic protection properties of TiO₂ nanotube arrays by simple surface UV treatment. *Appl Surf Sci* 394:440–445
14. Li J, Lin CJ, Lin CG (2011) A photoelectrochemical study of highly ordered TiO₂ nanotube arrays as the photoanodes for cathodic protection of 304 stainless steel. *J Electrochem Soc* 158:C55–C62
15. Li J, Yun H, Lin CJ (2007a) The Fe-doped TiO₂ nanotube arrays as a photoanode for cathodic protection of stainless steel. *Acta Phys-Chim Sin* 23:1886–1892
16. Lei CX, Feng ZD, Zhou H (2012) Visible-light-driven photogenerated cathodic protection of stainless steel by liquid-phase-deposited TiO₂ films. *Electrochim Acta* 68:134–140
17. Li J, Yun H, Lin CJ (2007b) A photoelectrochemical study of n-doped TiO₂ nanotube arrays as the photoanodes for cathodic protection of SS. *J Electrochem Soc* 154:C631–C636
18. Li J, Lin CJ, Lai YK, Du RG (2010) Photogenerated cathodic protection of flower-like, nanostructured, N-doped TiO₂ film on stainless steel. *Surf Coat Technol* 205:557–564
19. Xu AJ, Tu WG, Shen SJ, Lin ZP, Gao N, Zhong WW (2020) BiVO₄@MoS₂ core-shell heterojunction with improved photocatalytic activity for discoloration of Rhodamine B. *Appl Surf Sci* 528:146949–146955
20. Kirubasankar B, Palanisamy P, Arunachalam S, Murugadoss V, Angaiah S (2019) 2D MoSe₂-Ni(OH)₂ nanohybrid as an efficient electrode material with high rate capability for asymmetric supercapacitor applications. *Chem Eng J* 335:881–890
21. Sowbakkivavathi ES, Murugadoss V, Sittaramane R, Angaiah S (2020) Development of MoSe₂/PANI composite nanofibers as an alternative to Pt counter electrode to boost the photoconversion efficiency of dye sensitized solar cell. *J Solid State Electrochem* 24:2289–2300
22. Sun MM, Chen ZY (2015) Enhanced photoelectrochemical cathodic protection performance of the In₂O₃/TiO₂ composite. *J Electrochem Soc* 162:C96–C104
23. Liu Q, Hu J, Liang Y, Guan ZC, Zhang H, Wang HP, Du RG (2016) Preparation of MoO₃/TiO₂ composite films and their application in photoelectrochemical anticorrosion. *J Electrochem Soc* 163:C539–C544
24. Guan ZC, Wang HP, Wang X, Hu J, Du RG (2018) Fabrication of heterostructured β-Bi₂O₃-TiO₂ nanotube array composite film for photoelectrochemical cathodic protection applications. *Corros Sci* 136:60–69
25. Sun WX, Cui SW, Wei N, Chen SG, Liu YP, Wang DA (2018) Hierarchical WO₃/TiO₂ nanotube nanocomposites for efficient photocathodic protection of 304 stainless steel under visible light. *J Alloys Compd* 749:741–749
26. Zhou MJ, Zeng ZO, Zhong L (2009) Photogenerated cathode protection properties of nano-sized TiO₂/WO₃ coating. *Corros Sci* 51:1386–1391
27. Wang ZP, Xiao BB, Lin ZP, Shen SJ, Xu AJ, Du ZX, Chen YC, Zhong WW (2021) In-situ surface decoration of RuO₂ nanoparticles by laser ablation for improved oxygen evolution reaction activity in both acid and alkali solutions. *J Energy Chem* 54:510–518
28. Chueh YL, Hsieh CH, Chang MT, Chou L, Lao CS, Song JH, Gan JY, Wang ZL (2010) RuO₂ nanowires and RuO₂/TiO₂ core/shell nanowires: from synthesis to mechanical, optical, electrical, and photoconductive properties. *Adv Mater* 19:143–149
29. Ning XB, Ge SS, Wang XT, Li H, Li XR, Liu XQ, Huang YL (2017) Preparation and photocathodic protection property of Ag₂S-TiO₂ composites. *J Alloys Compd* 719:15–21
30. Hu J, Guan ZC, Liang Y, Zhou JZ, Liu Q, Wang HP, Zhang H, Du RG (2017) Bi₂S₃ modified single crystalline rutile TiO₂ nanorod array films for photoelectrochemical cathodic protection. *Corros Sci* 125:59–67
31. Singh N, Murugadoss V, Rajavedhanayagam J, Angaiah S (2019) A wide solar spectrum light harvesting Ag₂Se quantum dot-sensitized porous TiO₂ nanofibers as photoanode for high-performance QDSC. *J Nanopart Res* 21:176
32. Guo XQ, Liu W, Cao LX, Su G, Xu HM, Liu BH (2013) Graphene incorporated nanocrystalline TiO₂ films for the photocathodic protection of 304 stainless steel. *Appl Surf Sci* 283:498–504
33. Park JH, Park JM (2014) Photo-generated cathodic protection performance of electrochemically Co-deposited layers of TiO₂ nanoparticles and graphene nanoplatelets on steel substrate. *Surf Coat Technol* 258:62–71
34. Zhang WW, Guo HL, Sun HQ, Zeng RC (2016) Hydrothermal synthesis and photoelectrochemical performance enhancement of TiO₂/graphene composite in photo-generated cathodic protection. *Appl Surf Sci* 382:128–134
35. Xie X, Liu L, Chen RZ, Liu G, Li Y, Wang FH (2018) Long-term photoelectrochemical cathodic protection by Co(OH)₂-modified TiO₂ on 304 stainless steel in marine environment. *J Electrochem Soc* 165:H3154–H3163
36. Wang XT, Ning XB, Shao Q, Ge SS, Fei ZY, Lei J, Hou BR (2018) ZnFeAl-layered double hydroxides/TiO₂ composites as photoanodes for photocathodic protection of 304 stainless steel. *Sci Rep* 8:4116–4123
37. Kottayi R, Panneerselvam P, Singh N, Murugadoss V, Sittaramane R, Angaiah S (2020) Influence of bifunctional linker on loading of Cu₂AgInS₄ QDs onto porous TiO₂ NFs to use as an effective photoanode to boost up the photoconversion efficiency of QDSC. *New J Chem* 44:13148–13156
38. Kottayi R, Panneerselvam P, Murugadoss V, Sittaramane R, Angaiah S (2020) Cu₂AgInSe₄ QDs sensitized electrospun porous TiO₂ nanofibers as an efficient photoanode for quantum dot sensitized solar cells. *Sol Energy* 199:317–325
39. Singh N, Murugadoss V, Nemala S, Mallick S, Angaiah S (2018) Cu₂ZnSnSe₄ QDs sensitized electrospun porous TiO₂ nanofibers as photoanode for high performance QDSC. *Sol Energy* 171:571–579
40. Shi HX, Zhao YY, Fan J, Tang ZS (2019) Construction of novel Z-scheme flower-like Bi₂S₃/SnIn₄S₈ heterojunctions with enhanced visible light photodegradation and bactericidal activity. *Appl Surf Sci* 465:212–222
41. Yan TJ, Li LP, Li GS, Wang YJ, Hu WB, Guan XF (2011) Porous SnIn₄S₈ microspheres in a new polymorph that promotes dyes degradation under visible light irradiation. *J Hazard Mater* 186:272–279
42. Yan TJ, Li LP, Li GS (2011) Solvothermal synthesis of hierarchical SnIn₄S₈ microspheres and their application in photocatalysis. *Res Chem Intermed* 37:297–307
43. Deng F, Lu XY, Zhao LN, Luo YT, Pei XL, Luo XB, Luo SL (2016) Facile low-temperature co-precipitation method to synthesize hierarchical network-like g-C₃N₄/SnIn₄S₈ with superior photocatalytic performance. *J Mater Sci* 51:6998–7007
44. Xu B, He PL, Liu HL, Wang PP, Zhou G, Wang X (2014) A 1D/2D helical CdS/ZnIn₂S₄ nano-heterostructure. *Angew Chem Int Ed* 53:2339–2343
45. Deng XY, Zhang HX, Guo RN, Cui YQ, Ma QL, Zhang XY, Cheng XW, Li B, Xie MZ, Cheng QF (2018) Effect of fabricating parameters on photoelectrocatalytic performance of CeO₂/TiO₂ nanotube arrays photoelectrode. *Sep Purif Technol* 193:264–273
46. Jiang XH, Sun MM, Chen ZY, Jing JP, Feng C (2020) An ultrafine hyperbranched CdS/TiO₂ nanolawn photoanode with highly efficient photoelectrochemical performance. *J Alloys Compd* 816:152533–152543

47. Deng F, Zhong F, Zhao LN, Luo XB, Luo SL, Dionysiou DD (2017) One-step in situ hydrothermal fabrication of octahedral CdS/SnIn₄S₈ nano-hetero-junction for highly efficient photocatalytic treatment of nitrophenol and real pharmaceutical wastewater. *J Hazard Mater* 340:85–95
48. Wang L, Li XY, Teng W, Zhao QD, Shi Y, Yue RL, Chen YF (2013) Efficient photocatalytic reduction of aqueous Cr(VI) over flower-like SnIn₄S₈ microspheres under visible light illumination. *J Hazard Mater* 244:681–688
49. Dai GP, Yu JG, Liu G (2011) Synthesis and enhanced visible-light photoelectrocatalytic activity of p–n junction BiOI/TiO₂ nanotube arrays. *J Phys Chem C* 115:7339–7346
50. Sun DD, Hao YX, Wang CY, Zhang XH, Yu XF, Yang XJ, Li LL, Lu ZM, Shang W (2020) TiO₂-CdS supported CuNi nanoparticles as a highly efficient catalyst for hydrolysis of ammonia borane under visible-light irradiation. *Int J Hydrogen Energy* 45:4390–4402
51. Roy P, Berger S, Schmuki P (2011) TiO₂ nanotubes: synthesis and applications. *Angew Chem Int Ed* 50:2904–2939
52. Shi H, Wang C, Zhao Y, Liu E, Fan J, Ji Z (2019) Highly efficient visible light driven photocatalytic inactivation of *E. coli* with Ag QDs decorated Z-scheme Bi₂S₃/SnIn₄S₈ composite. *Appl Catal B Environ* 254:403–413
53. Xu PF, Huang SY, Liu MH, Lv YC, Wang ZH, Long JL, Zhang W, Fan HJ (2019) Z-Schemed WO₃/rGO/SnIn₄S₈ sandwich nanohybrids for efficient visible light photocatalytic water purification. *Catalysts* 9:187–202
54. Sun MM, Chen ZY, Li JR, Hou J, Xu FL, Xu LK, Zeng RC (2018) Enhanced visible light-driven activity of TiO₂ nanotube array photoanode co-sensitized by “green” AgInS₂ photosensitizer and In₂S₃ buffer layer. *Electrochim Acta* 269:429–440
55. Sun WX, Wei N, Cui HZ, Lin Y, Wang XZ, Tian J, Li J, Wen J (2018) 3D ZnIn₂S₄ nanosheet/TiO₂ nanowire arrays and their efficient photocathodic protection for 304 stainless steel. *Appl Surf Sci* 434:1030–1039
56. Liu Q, Lu H, Shi ZW, Wu FL, Guo J, Deng KM, Li L (2014) 2D ZnIn₂S₄ nanosheet/1D TiO₂ nanorod heterostructure arrays for improved photoelectrochemical water splitting. *ACS Appl Mater Interfaces* 6:17200–17207
57. Wang X, Guan ZC, Jin P, Tang YY, Song GL, Liu GK, Du RG (2019) Facile fabrication of BiVO₄ modified TiO₂ nanotube film photoanode and its photocathodic protection effect on stainless steel. *Corros Sci* 157:247–255
58. Shen GX, Chen YC, Lin CJ (2005) Corrosion protection of 316 L stainless steel by a TiO₂ nanoparticle coating prepared by sol–gel method. *Thin Solid Films* 489:130–136
59. Liu WJ, Yin KC, He F, Ru QX, Zuo SX, Yao C (2019) A highly efficient reduced graphene oxide/SnO₂/TiO₂ composite as photoanode for photocathodic protection of 304 stainless steel. *Mater Res Bull* 113:6–13
60. Sun ZX, Li FY, Zhao ML, Xu L, Fang SN (2013) A comparative study on photoelectrochemical performance of TiO₂ photoanodes enhanced by different polyoxometalates. *Electrochem Commun* 30:38–41
61. Sun MM, Chen ZY, Yu JQ (2013) Highly efficient visible light induced photoelectrochemical anticorrosion for 304 SS by Ni-doped TiO₂. *Electrochim Acta* 109:13–19

Publisher's Note

Springer Nature remains neutral with regard to jurisdictional claims in published maps and institutional affiliations.

Submit your manuscript to a SpringerOpen[®] journal and benefit from:

- Convenient online submission
- Rigorous peer review
- Open access: articles freely available online
- High visibility within the field
- Retaining the copyright to your article

Submit your next manuscript at ► [springeropen.com](https://www.springeropen.com)
